ECG Modeling for Simulation of Arrhythmias in Time-Varying Conditions

Lorenzo Bachi, Hesam Halvaei, Cristina Pérez, Alba Martín-Yebra, Andrius Petrėnas, Andrius Sološenko, Linda Johnson, Vaidotas Marozas, *Member, IEEE*, Juan Pablo Martínez, Esther Pueyo, Martin Stridh, Pablo Laguna, *Fellow, IEEE*, and Leif Sörnmo, *Fellow, IEEE*

***Abstract*—The present article proposes an ECG simulator that advances modeling of arrhythmias and noise by introducing time-varying signal characteristics. The simulator is built around a discrete-time Markov chain model for simulating atrial and ventricular arrhythmias of particular relevance when analyzing atrial fibrillation (AF). Each state is associated with statistical information on episode duration and heartbeat characteristics. Statistical, time-varying modeling of muscle noise, motion artifacts, and the influence of respiration is introduced to increase the complexity of simulated ECGs, making the simulator well suited for data augmentation in machine learning. Modeling of how the PQ and QT intervals depend on heart rate is also introduced. The realism of simulated ECGs is assessed by three experienced doctors, showing that simulated ECGs are difficult to distinguish from real ECGs. Simulator usefulness is illustrated in terms of AF detection performance when either simulated or real ECGs are used to train a neural network for signal quality control. The results show that both types of training lead to similar performance.**

***Index Terms*—Arrhythmias, ECG signals, noise, respiration, simulation models.**

Manuscript received 3 February 2023; revised 9 June 2023; accepted 14 June 2023. Date of publication 22 June 2023; date of current version 22 November 2023. The work was supported in part by the Royal Physiographic Society, Lund, Sweden, in part by CIBERBBN through Instituto de Salud Carlos III and FEDER (Spain), in part by Gobierno de Aragón (BSICoS T39-17R), in part by MICINN under Projects PID2019104881RB-I00 and PID2019105674RB-I00, and in part by the European Regional Development Fund through an agreement with the Research Council of Lithuania under Grant 01.2.2-LMT-K-718-03-0027. *(Corresponding author: Lorenzo Bachi.)*

Lorenzo Bachi is with the Institute of Life Sciences, Sant'Anna School of Advanced Studies, 56127 Pisa, Italy (e-mail: l.bachi@santannapisa.it).

Hesam Halvaei, Martin Stridh, and Leif Sörnmo are with the Department of Biomedical Engineering, Lund University, Sweden.

Cristina Pérez, Alba Martín-Yebra, Juan Pablo Martínez, Esther Pueyo, and Pablo Laguna are with the Biomedical Signal Interpretation & Computational Simulation Group, Aragón Institute of Engineering Research, Zaragoza University, Spain, and also with the CIBER-BBN, Spain.

Andrius Petrėnas, Andrius Sološenko, and Vaidotas Marozas are with the Biomedical Engineering Institute, Kaunas University of Technology, Lithuania.

Linda Johnson is with the Department of Clinical Physiology, Skåne University Hospital and Department of Clinical Sciences, Malmö, Lund University, Sweden.

Digital Object Identifier 10.1109/TBME.2023.3288701

I. Introduction

SIMULATED ECG signals have since long proven useful for investigating crucial performance aspects of signal processing methods under controlled conditions, ranging from simple test signals to signals with composite characteristics, exemplified by models for simulating maternal and fetal ECGs [1], [2], [3], T wave alternans [4], and paroxysmal atrial fibrillation (AF) [5]. These simulators have in common that they are based on mathematical models of relevant physiological phenomena, while they do not pretend to model biophysical mechanisms.

An emerging application of simulation is found in training of classifiers developed for, e.g., ECG-based localization of atrial flutter substrates [6], and photoplethysmogram-based detection of brady- and tachycardia [7]. Once trained, classifier performance may be tested on real signals. An important incentive for training on simulated data is the scarcity of huge annotated datasets; however, it remains to be shown whether the necessary level of simulator sophistication can be achieved to make training fully sustainable.

In the context of AF analysis, simulated ECGs have been used to gain insight on how physiological and technical factors influence detection performance with respect to, e.g., episode duration, lead selection, and noise level [8], [9]. Depending on the type of detector, i.e., whether rhythm-only, rhythm and morphology, or segments of raw samples are explored, these factors can have considerable influence on performance. Similar insights are decidedly more difficult to achieve when using annotated real ECGs. Another application of simulated ECGs is performance evaluation of methods for f wave extraction [10], [11], [12].

In several clinical studies, brief episodes of atrial tachycardia (AT) and atrial runs have been associated with increased risk of stroke beyond incident AF [13], [14]. Modeling of AT and atrial runs, which so far has not received any attention in the literature, may help uncover weaknesses of their algorithmic detection. Moreover, ventricular ectopic beats (VPBs), bigeminy, and trigeminy are of equal interest to model as they represent important sources of falsely detected AF episodes. Increased complexity of simulated ECGs should lead to results closer to real-world performance than those obtained from simulated ECGs which have been restricted to transitions between sinus rhythm (SR) and AF.

Noise modeling is an essential part of any simulator aiming to generate realistic signals which can challenge the performance of a method. To account for time-varying spectral characteristics, time-varying autoregressive (AR) models driven by white, Gaussian noise have been proposed for modeling of baseline

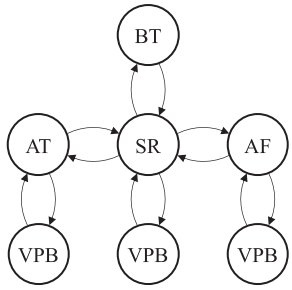

Fig. 1. Markov chain modeling of arrhythmias, comprising atrial tachycardia (AT), bi-/trigeminy (BT), atrial fibrillation (AF), ventricular premature beat (VPB), and sinus rhythm (SR). Each arrow is associated with a transition probability.

wander [1] and muscle noise [2]. In those studies, most model parameters were estimated from the PhysioNet MIT–BIH Noise Stress Test Database (NSTDB), resulting either in time-varying filter parameter estimates [1] or fixed filter parameter estimates made time-varying by letting the position of related pole pairs vary according to a random walk model [2]. Concerning motion artifacts, a time-invariant filtered white noise approach was recently proposed for simulating textile sensor noise, assuming a heavy-tailed, non-Gaussian probability density function (PDF) of the white noise [15]. In ambulatory monitoring and exercise stress testing, where motion artifacts can resemble heartbeats, such an approach is unsuitable as white noise is a stationary process.

The present article extends considerably the simulation model for paroxysmal AF proposed in [5] by modeling atrial and ventricular arrhythmias of particular relevance for AF analysis (Sections III and IV). Novel approaches to statistical, time-varying modeling of muscle noise, motion artifacts, and the influence of respiration are presented, which serves to increase the complexity of simulated ECGs, of particular relevance for training machine learning models (Sections V and VII). Moreover, the proposed simulator accounts for how PQ and QT intervals depend on heart rate (Section VIII). The realism of simulated ECGs is assessed by three experienced medical doctors, and the usefulness of the simulator is illustrated by evaluating AF detection performance using either real or simulated ECGs for training (Section IX). While simulated ECGs in [5] were composed of either synthetic or real components, the present study deals only with synthetic components as real ones are unsuitable for modeling of time-varying conditions.

The simulator code is freely available at [16].

II. Arrhythmia Modeling Framework

Transitioning between episodes of SR, AF, AT, and bi- and trigeminy (BT) is modeled by a discrete-time Markov chain, defined so that any of these arrhythmias is followed by SR, see Fig. 1; see Section XI for a discussion of the Markov model definition. The transitioning is defined by probabilities, whereas the duration of episodes are defined by rhythm-specific probability mass functions (PMFs) expressed in number of beats. Hence, when simulating an ECG signal, the total duration of a certain rhythm depends on the transition probabilities as well as the properties of the PMFs. The multiple VPB states reflect that an isolated VPB can occur in SR, AT, and AF, but not in BT; thus, a VPB does not have to be followed by SR. Unlike a VPB, which is modeled by its own state, an atrial premature beat (APB) belongs to the AT state and has a one-beat duration. In certain states, a number of probabilistic decisions have to be made, e.g., the type of APB or VPB to occur.

The durations of SR and AF episodes are modeled by their respective exponential PMFs, combined with a criterion to exclude episodes with few beats. The modeling of AT, VPBs, and BT are described below in Sections III and IV.

The transition probabilities $p_{\mathrm{SR}\to\mathrm{AF}}$, $p_{\mathrm{SR}\to\mathrm{AT}}$, $p_{\mathrm{SR}\to\mathrm{BT}}$, $p_{\mathrm{SR}\to\mathrm{VPB}}$, $p_{\mathrm{AF}\to\mathrm{VPB}}$, $p_{\mathrm{AT}\to\mathrm{VPB}}$, $p_{\mathrm{AT}\to\mathrm{SR}}$, and $p_{\mathrm{AF}\to\mathrm{SR}}$ are set to values in the interval [0,1], whereas $p_{\mathrm{BT}\to\mathrm{SR}}$, $p_{\mathrm{VPB}\to\mathrm{AT}}$, $p_{\mathrm{VPB}\to\mathrm{SR}}$, and $p_{\mathrm{VPB}\to\mathrm{AF}}$ are all set to 1. Rather than directly defining the first-mentioned set of transition probabilities, they can be defined in a more intuitive way by extending the well-established notion of AF burden B_{AF}, i.e., the percentage of time spent in AF during the monitored period, to also apply to the other arrhythmias, i.e., the burdens B_{AT}, B_{VPB}, and B_{BT}. Using the four burdens in combination with the mean episode durations, the transition probabilities can be determined, see Appendix A for details.

III. Modeling of Atrial Arrhythmias

Two public, annotated databases, the MIT–BIH Arrhythmia Database and the MIT–BIH Supraventricular Arrhythmia Database [17], were analyzed to determine certain model characteristics. The former database is annotated with respect to beat type and rhythm, whereas the latter database makes no distinction between atrial and nodal supraventricular beats and therefore both types of beat are jointly analyzed.

A. Atrial Premature Beats

1) Rhythm: The RR intervals immediately preceding and following an isolated APB, denoted $d_{\mathrm{RR,p}}$ and $d_{\mathrm{RR,f}}$, respectively, are related to the current RR interval d_{RR} in SR, but modified by a positive-valued, uniformly distributed parameter β that depends on the type of APB. Expanding on the model in [5], the following rules apply to generate $d_{\mathrm{RR,p}}$ and $d_{\mathrm{RR,f}}$:

- *APB with sinus node reset (APB1):* $d_{\mathrm{RR,p}} = \beta_{\mathrm{APB1,p}} d_{\mathrm{RR}}$, $d_{\mathrm{RR,f}} = d_{\mathrm{RR}}$;
- *APB with delayed sinus reset (APB2):* $d_{\mathrm{RR,p}} = \beta_{\mathrm{APB2,p}} d_{\mathrm{RR}}$, $d_{\mathrm{RR,f}} = \beta_{\mathrm{APB2,f}} d_{\mathrm{RR}}$;
- *APB with compensatory pause (APB3):* $d_{\mathrm{RR,p}} = \beta_{\mathrm{APB3,p}} d_{\mathrm{RR}}$, $d_{\mathrm{RR,f}} = (2 - \beta_{\mathrm{APB3,p}}) d_{\mathrm{RR}}$;
- *Interpolated APB (APB4):* $d_{\mathrm{RR,p}} = \beta_{\mathrm{APB4,p}} d_{\mathrm{RR}}$, $d_{\mathrm{RR,f}} = (1 - \beta_{\mathrm{APB4,p}}) d_{\mathrm{RR}}$; occurs only when $d_{\mathrm{RR}} > 400$ ms,

where $\beta_{\mathrm{APB1,p}}$, $\beta_{\mathrm{APB2,p}}$, $\beta_{\mathrm{APB3,p}}$, and $\beta_{\mathrm{APB4,p}}$ are all < 1 except $\beta_{\mathrm{APB2,f}} > 1$. Each type of APB is associated with a probability of occurrence $p_{\mathrm{APB}i}$, $i = 1, 2, 3, 4$.

2) Morphology: The P wave and the QRST complex of an APB are modeled by Hermite functions (see below for definition) and Gaussian functions, respectively [5]. Since the depolarization of atrial tissue differs between a sinus beat and an APB, different sets of parameter values are used to generate the respective P waves.

B. Atrial Tachycardia

The main types of AT are either focal, multifocal, or reentrant, of which the first two are subject to modeling since both are paroxysmal and occur as transitional rhythms between frequent

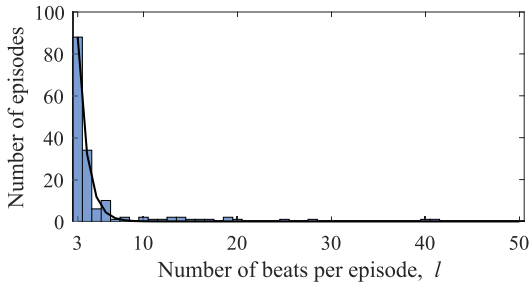

Fig. 2. Histogram of atrial tachycardia episode duration and the fitted probability mass function $p_{\mathrm{AT}}(l)$ (solid line) proportional to $e^{-b_{\mathrm{AT}}l}$.

APBs and AF [18]. Focal AT originates from a single ectopic focus within the atria and is defined by a heart rate exceeding 100 beats per minute (BPM), a regular rhythm, and a non-sinus P-wave morphology that remains the same throughout an AT episode. Multifocal AT originates from multiple ectopic foci and is also defined by a higher than normal heart rate, however, the rhythm is irregular with varying RR and PR intervals and at least three distinct, non-sinus P-wave morphologies. Although the model puts emphasis on focal AT, multifocal AT can, if desired, be easily modeled using a different set of parameter values.

Fig. 2 presents the histogram of AT episode duration obtained from the two above-mentioned public databases combined, highlighting an inversely proportional relation between the number of episodes and episode duration l, expressed in number of beats. This relation is modeled by a PMF $p_{\mathrm{AT}}(l)$ accounting not only for AT episodes ($l \geq 3$), but also for isolated APB ($l = 1$) and atrial couplets (ACs, $l = 2$):

$$p_{\mathrm{AT}}(l) = \begin{cases} p_{\mathrm{APB}}, & l = 1; \\ p_{\mathrm{AC}}, & l = 2; \\ a_{\mathrm{AT}} e^{-b_{\mathrm{AT}} l}, & l = 3, \ldots, 50; \\ 0, & \text{otherwise.} \end{cases} \tag{1}$$

Based on the two databases, the maximum episode duration is set to 50 beats. The constant a_{AT} ensures that $p_{\mathrm{AT}}(l)$ sums to 1, and the decay b_{AT} is estimated using least squares (LS) fitting of $p_{\mathrm{AT}}(l), l = 3, 4, \ldots, 50$, to the histogram in Fig. 2.

The RR intervals immediately preceding and following an episode are given by $d_{\mathrm{RR,p}} = \beta_{\mathrm{AT,p}} d_{\mathrm{RR}}$ and $d_{\mathrm{RR,f}} = \beta_{\mathrm{AT,f}} d_{\mathrm{RR}}$, whereas the RR intervals within an episode are given by

$$d_{\mathrm{RR},i} = \beta_{\mathrm{AT}} d_{\mathrm{RR}} + \Delta d_{\mathrm{RR},i}, \quad i = 1, \ldots, l. \tag{2}$$

The parameters $\beta_{\mathrm{AT,p}}$, $\beta_{\mathrm{AT,f}}$, β_{AT}, and $\Delta d_{\mathrm{RR},i}$ are modeled by uniform PDFs whose limits are determined from the public databases. The uniform PDF of β_{AT} is based on the ratio between the average of the three RR intervals immediately preceding AT and the average of the RR intervals within an AT episode. Whenever $d_{\mathrm{RR},i}$ in (2) is shorter than 300 ms, another $\Delta d_{\mathrm{RR},i}$ is generated until $d_{\mathrm{RR},i}$ exceeds 300 ms.

IV. Modeling of Ventricular Arrhythmias

A. Ventricular Premature Beats

1) Rhythm: A VPB is a single-beat arrhythmia and therefore not associated with a PMF. The two RR intervals immediately preceding and following a VPB, i.e., $d_{\mathrm{RR,p}}$ and $d_{\mathrm{RR,f}}$, are based on the current RR interval d_{RR}, generated as follows:

- *VPB with compensatory pause (VPB1):* $d_{\mathrm{RR,p}} = \beta_{\mathrm{VPB1,p}} d_{\mathrm{RR}}$, $d_{\mathrm{RR,f}} = (2 - \beta_{\mathrm{VPB1,p}}) d_{\mathrm{RR}}$;
- *VPB with noncompensatory pause and sinus node reset (VPB2):* $d_{\mathrm{RR,p}} = \beta_{\mathrm{VPB2,p}} d_{\mathrm{RR}}$, $d_{\mathrm{RR,f}} = d_{\mathrm{RR}}$;
- *Interpolated VPB (VPB3):* $d_{\mathrm{RR,p}} = \beta_{\mathrm{VPB3,p}} d_{\mathrm{RR}}$, $d_{\mathrm{RR,f}} = (1 - \beta_{\mathrm{VPB3,p}}) d_{\mathrm{RR}}$; occurs only when $d_{\mathrm{RR}} > 400$ ms,

where $\beta_{\mathrm{VPB1,p}}, \beta_{\mathrm{VPB2,p}}$, and $\beta_{\mathrm{VPB3,p}}$ are all <1 and uniformly distributed over an interval determined by established medical knowledge. Each type of VPB is associated with a probability of occurrence $p_{\mathrm{VPB}i}, i = 1, 2, 3..$ In AF and AT, VPB2 can only occur.

2) Morphology: The QRS complex and the T wave of a VPB are modeled by their respective linear combinations of the orthonormal Hermite functions $\varphi_j(t)$ [19], [20], [21], defined by

$$x(t; \tau, \sigma) = \sum_{j=0}^{J-1} c_j(\tau, \sigma) \varphi_j(\sigma(t - \tau)), \tag{3}$$

where

$$\varphi_j(t) = H_j(t)(2^j j! \sqrt{\pi})^{-1/2} e^{-t^2/2}, \tag{4}$$

J is the number of functions, and $c_j(\tau, \sigma)$, σ, and τ denote amplitude, width, and position, respectively. The Hermite polynomials are recursively given by $H_j(t) = 2tH_{j-1}(t) - 2(j-1)H_{j-2}(t), j > 2$, with $H_0(t) = 1$ and $H_1(t) = 2t$. Due to orthonormality, only two 2-dimensional optimization problems need to be solved when fitting the Hermite functions to data, one for the QRS complex and another for the T-wave, whereas a 2 J-dimensional problem when fitting Gaussian functions as done in, e.g., [1], [22], [23].

The segmentation of a VPB into QRS complex and T wave may introduce a jump at the boundary, especially for sloping ST segments. However, the jump may be reduced by adding a logistic function to the model [24],

$$s(t; c_s, \sigma_s, \tau_s) = \frac{c_s}{1 + e^{-\sigma_s(t - \tau_s)}}, \tag{5}$$

where c_s, σ_s, and τ_s denote amplitude, steepness, and position, respectively.

To fit the Hermite and the logistic functions to a real 12-lead VPB, the model parameters in (3) and (5) are estimated using an efficient LS-based, iterative method described in Appendix B. Then, the simulated X, Y, Z leads are obtained by applying regression transformation to the simulated 12-lead VPB [25]. Thus, this approach differs from the one in [5] where the simulated 12-lead beat was obtained by applying the Dower transformation to the simulated X, Y, and Z leads.

B. Bigeminy and Trigeminy

Modeling of VPBs facilitates modeling of bigeminy, i.e., every second beat is a VPB, and trigeminy, i.e., every third beat is a VPB. Markov chain modeling of transitions between SR and BT is similar to that of SR and AT, except that a transition from SR to BT is accompanied by a decision on whether bigeminy or trigeminy should occur. The probability of bigeminy to occur relative to trigeminy, denoted p_{B}, is determined from the MIT–BIH Arrhythmia Database (MITADB); thus, the probability of trigeminy is $(1 - p_{\mathrm{B}})$.

This database was also used to compute the histogram of BT episode duration, i.e., the durations of bi- and trigeminy

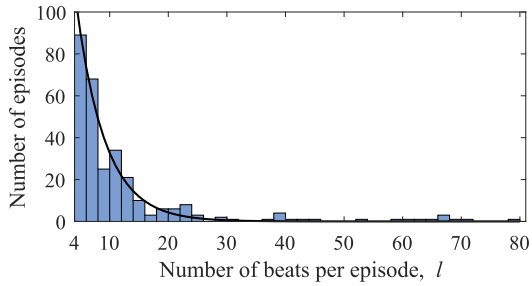

Fig. 3. Histogram of bi- and trigeminy episode duration and the fitted probability mass function $p_{\mathrm{BT}}(l)$ (solid line) proportional to $e^{-b_{\mathrm{BT}}l}$.

episodes combined into one histogram, see Fig. 3. Similar to the AT histogram in Fig. 2, the BT histogram highlights an inversely proportional relation between the number of episodes and episode duration l, modeled by the following PMF:

$$p_{\mathrm{BT}}(l) = \begin{cases} a_{\mathrm{BT}} e^{-b_{\mathrm{BT}} l}, & l = 4, \ldots, 80; \\ 0, & \text{otherwise.} \end{cases} \tag{6}$$

From the database, the default minimum and maximum episode duration were found to be 4 and 80, respectively, and the LS estimate of the decay b_{BT} was determined. The constant a_{BT} ensures that $p_{\mathrm{BT}}(l)$ sums to 1.

When a transition from SR to BT occurs, the episode duration is sampled from the PMF in (6). For bigeminy, sinus beats and VPBs are placed one after the other, whereas, in trigeminy, a VPB follows every other two sinus beats. In both bi- and trigeminy, the RR intervals immediately preceding and following a VPB are changed by $\beta_{\mathrm{BT,p}}$ and $\beta_{\mathrm{BT,f}}$, respectively, whereas, in trigeminy, the RR interval between the two sinus beats is based on the current RR interval d_{RR}. The uniform distributions of $\beta_{\mathrm{BT,p}}$ and $\beta_{\mathrm{BT,f}}$ were determined by statistical analysis of bi- and trigeminy episodes in MITADB.

V. Modeling of Time-Varying Noise

The modeling of muscle noise and motion artifacts, commonly observed in ambulatory monitoring and exercise stress testing, is paid special attention. The filtered white noise approach, mentioned in the introduction, serves as the starting point, but altered in several respects to account for prominent characteristics such as a time-varying level of muscle noise and a random occurrence pattern and randomly changing shape of QRS-like motion artifacts. Hence, the noise added to the noise-free ECG is assumed to consist of muscle noise $x_{\mathrm{MN}}(n)$ and motion artifacts $x_{\mathrm{MA}}(n)$; concerning the modeling of baseline wander, see Section XI. It should be noted that each lead is corrupted by individual noise realizations, and, consequently, no interlead correlation is introduced in the simulated ECG.

A. Muscle Noise

Muscle noise $x_{\mathrm{MN}}(n)$ is modeled as a nonstationary AR(p) process, defined by the following difference equation:

$$x_{\mathrm{MN}}(n) = a_{1,n} x_{\mathrm{MN}}(n-1) + \cdots + a_{p,n} x_{\mathrm{MN}}(n-p) + w(n), \tag{7}$$

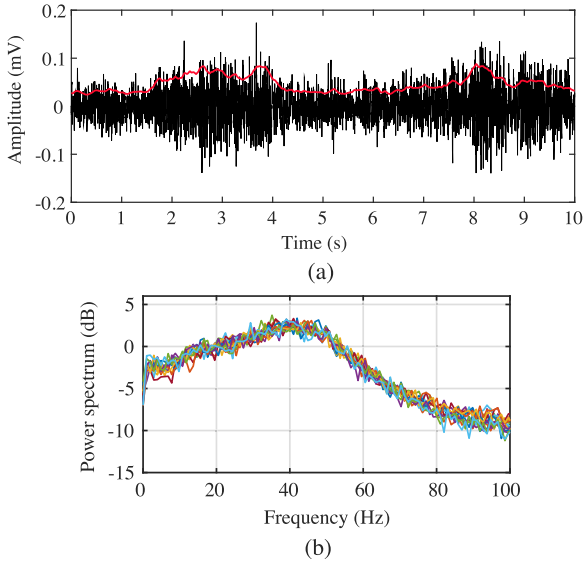

Fig. 4. Typical examples of (a) time-varying muscle noise (the envelope is displayed in red), and (b) several superimposed muscle noise power spectra (logarithmic scale) displayed up to 100 Hz, computed in successive 1-min intervals. Analyzed signals were recorded during exercise stress testing [26].

where $w(n)$ is white, Gaussian noise with time-varying variance $\sigma_w^2(n)$ and p is the model order. The time-varying parameters $a_{1,n}, \ldots, a_{p,n}$ are estimated using a two-step procedure. Firstly, the parameters of a stationary AR(p) model, i.e., $a_1, \ldots, a_p$, are estimated using amplitude-normalized, PQRST-cancelled ECGs recorded during exercise stress testing [26]. Amplitude normalization, accomplished by means of the envelope of the cancelled signal, is motivated by the large variation in noise level. Since the spectral content of muscle noise is confined to frequencies well below 100 Hz, parameter estimation is performed on signals sampled at a rate of 200 Hz to ensure a low-order AR model, taken to be $p = 4$. Hence, the sampling rate of the model output needs to be increased to the rate of the simulated ECG (1000 Hz). Secondly, the poles related to $\hat{a}_1, \ldots, \hat{a}_p$ are made time-varying using a simple random walk model [2].

While the spectral properties of muscle noise do not vary much over time, the noise level itself can vary considerably—two characteristics illustrated by Fig. 4. The following first-order model of how the standard deviation $\sigma_w(n)$ of $w(n)$ in (7) varies over time is proposed:

$$x_{\sigma_w}(n+1) = \nu x_{\sigma_w}(n) + v_{\sigma_w}(n), \tag{8}$$

$$\sigma_w(n) = \max(\sigma_{w,\min}, m_{\sigma_w}(n) + x_{\sigma_w}(n)), \tag{9}$$

where $v_{\sigma_w}(n)$ is white, Gaussian noise with variance σ_v^2; thus, the variance σ_x^2 of $x_{\sigma_w}(n)$ is $\sigma_x^2 = \sigma_v^2/(1-\nu^2)$. The initial value $x_{\sigma_w}(0)$ is set to 0 and the filter parameter ν is constrained to [0,1]. The standard deviation $\sigma_w(n)$ is composed of $m_{\sigma_w}(n)$, defining the mean noise level of the simulated ECG, and $x_{\sigma_w}(n)$, defining its variation. While a constant mean noise level is used as default, i.e., $m_{\sigma_w}(n) \equiv m_{\sigma_w}$, other definitions are certainly possible, e.g., to let $m_{\sigma_w}(n)$ gradually increase over time to mimic the noise profile of an exercise stress test. The half-wave

rectifier in (9) is introduced to ensure that $\sigma_w(n)$ exceeds a certain minimum level $\sigma_{w,\min}$.

B. Motion Artifacts

The starting point for modeling motion artifacts is a train of sparsely, randomly occurring spikes of different amplitudes defined by a Bernoulli–Gaussian process, i.e., the spike train, denoted $y(n)$, is the product of a binary-valued Bernoulli process $b(n)$ and white, Gaussian noise $z(n)$ with a uniformly distributed variance σ_z^2 [27]. The PMF of $b(n)$ is defined by

$$p(b(n)) = \begin{cases} p_b, & b(n) = 1; \\ 1 - p_b, & b(n) = 0, \end{cases} \tag{10}$$

where the probability p_b is uniformly distributed. To mimic the shape of motion artifacts, $y(n)$ is fed to a filter whose impulse response changes from spike to spike in a random fashion. The impulse response associated with the k:th spike, denoted $h_k(n;\boldsymbol{\theta}_k)$, is defined by an exponentially increasing part, lasting up to sample K_k, followed by an exponentially decreasing part lasting up to the filter length $L-1$,

$$h_k(n;\boldsymbol{\theta}_k) = \begin{cases} \alpha_{1,k}^{-n}, & n = 0,\ldots,K_k-1; \\ \alpha_{1,k}^{-K_k}\alpha_{2,k}^{n-K_k}, & n = K_k,\ldots,L-1, \end{cases} \tag{11}$$

where $\boldsymbol{\theta}_k = [\alpha_{1,k}, \alpha_{2,k}, K_k]$ with $0 \ll \alpha_{1,k}, \alpha_{2,k} < 1$ and $0 \ll K_k \ll L-1$. The parameters K_k, $\alpha_{1,k}$, and $\alpha_{2,k}$ change from spike to spike according to uniform PDFs.

To make the output of $h_k(n;\boldsymbol{\theta}_k)$, denoted $u(n)$, smoother and more realistic-looking, $u(n)$ is bandpass filtered using a linear filter with infinite impulse response, yielding

$$x_{\mathrm{MA}}(n) = b_{1,n}x_{\mathrm{MA}}(n-1) + \cdots + b_{q,n}x_{\mathrm{MA}}(n-q) + u(n), \tag{12}$$

where $b_{1,n},\ldots,b_{p,n}$ are chosen so that the cutoff frequencies of the filter are positioned at about 10 and 80 Hz and q set to 4. Similar to (7), the poles of $b_{1,n},\ldots,b_{q,n}$ vary over time according to the above-mentioned random walk model.

Motion artifacts observed in recordings made during handheld AF screening are typically broader in time and more pronounced than those observed in ambulatory monitoring and exercise stress testing modeled by (12). A simple approach to modeling the former type of artifacts is to integrate the output in (12), resulting in the following difference equation:

$$\begin{aligned} x_{\mathrm{MA}}(n) = {} & x_{\mathrm{MA}}(n-1) + b_{1,n}\Delta x_{\mathrm{MA}}(n-1) + \cdots \\ & + b_{q,n}\Delta x_{\mathrm{MA}}(n-q) + u(n), \end{aligned} \tag{13}$$

$$\Delta x_{\mathrm{MA}}(n) = x_{\mathrm{MA}}(n) - x_{\mathrm{MA}}(n-1). \tag{14}$$

The model in (13) is identical to the one in (12), except that $x_{\mathrm{MA}}(n)$ is replaced by $\Delta x_{\mathrm{MA}}(n)$ due to the integration.

VI. Arrhythmia and Noise Modeling: Examples

Arrhythmia modeling is illustrated by Fig. 5, displaying episode patterns with SR, AT, and AF, and Fig. 6, displaying low-noise ECGs with VPB, APB, AT, AF, and BT.

Noise modeling is illustrated in Fig. 7 by simulated, single-lead ECGs paired with similar-looking real ECGs extracted from recordings made during exercise stress testing, ambulatory monitoring, and handheld AF screening.

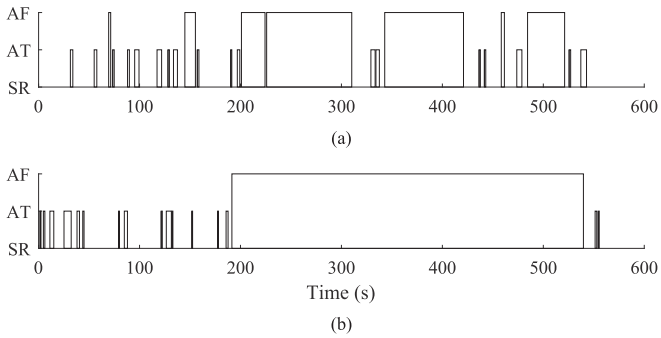

Fig. 5. Simulated episode patterns consisting of sinus rhythm (SR), atrial tachycardia (AT), and atrial fibrillation (AF), generated using arrhythmia burdens $B_{\mathrm{AT}} = 0.05$ and $B_{\mathrm{AF}} = 0.5$, and mean episode durations $e_{\mathrm{AT}} = 5$ beats and either (a) $e_{\mathrm{AF}} = 50$ beats or (b) $e_{\mathrm{AF}} = 300$ beats; see Appendix A for parameter definitions.

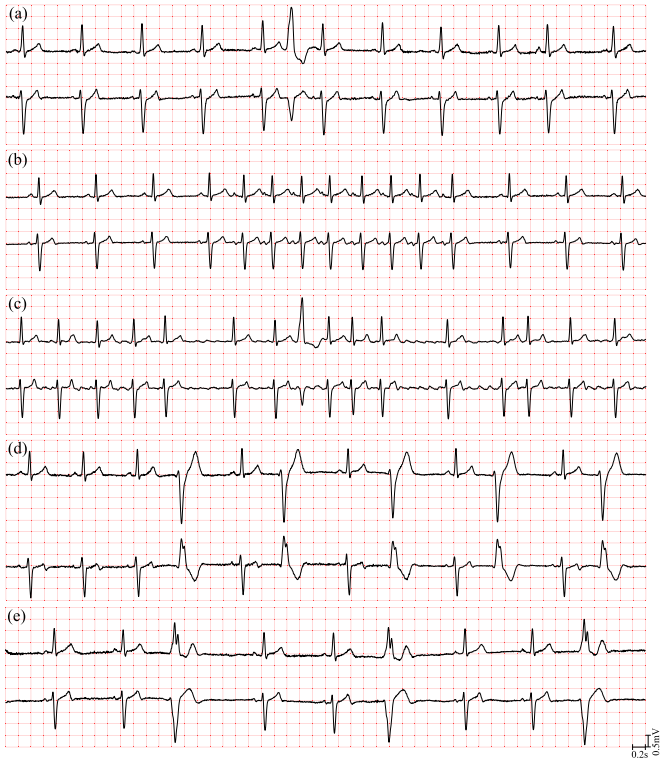

Fig. 6. Simulated 10-s, low-noise ECGs in leads II (top) and V_1 (bottom). (a) Interpolated ventricular premature beat (VPB) and atrial premature beat in sinus rhythm, (b) atrial tachycardia, (c) VPBs in atrial fibrillation, (d) ventricular bigeminy, and (e) ventricular trigeminy. Displayed leads are the same as those of the MIT-BIH Arrhythmia and Supraventricular Arrhythmia Databases.

VII. Modeling the Influence of Time-Varying Respiration

Respiration is manifested in the ECG by relatively periodic changes in the electrical axis of the heart as well as changes in heart rate. Since the respiratory frequency depends on the degree of physical effort, the assumption of a fixed respiratory frequency in [5] is generalized to become time-varying. Changes in heart rate due to respiration are modeled by a time-varying respiratory component of the heart rate variability (HRV) power

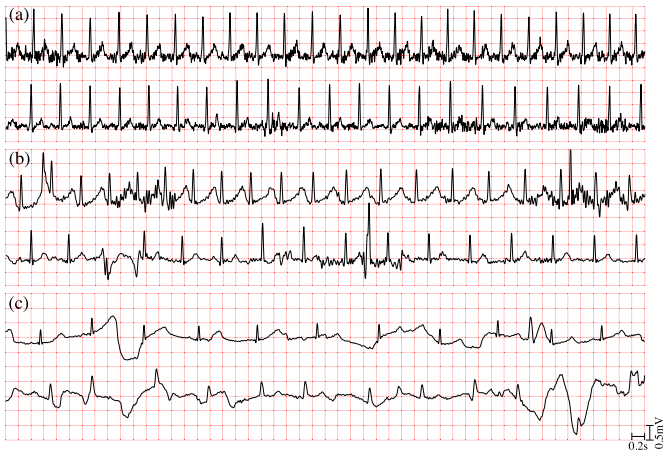

Fig. 7. Single-lead, 10-s simulated ECGs (top) and similar-looking real ECGs (bottom) with (a) muscle noise, (b) motion artifacts, common in ambulatory monitoring and exercise stress testing, with muscle noise added, and (c) motion artifacts common in handheld AF screening. Simulated ECGs are generated using (7), (12), and (13), respectively. ECGs in (c) are highpass filtered to facilitate presentation.

spectrum. While changes in heart rate are present in SR only, changes in the electrical axis, modeled by rotation of the VCG loop, are present also in arrhythmia.

The starting point is the respiratory interval tachogram, i.e., a series of successive respiration intervals $T_{r,0}, T_{r,1}, \ldots$, which can be transformed to a time-varying respiratory frequency $F_r(t)$ through the use of the inverse interval function [28].

A. Morphology Influenced by Time-Varying Respiration

The simulated, noise-free VCG signal $\mathbf{u}_{\rm VCG}(t)$ is transformed by rotation, defined by the product of three planar rotations around each of the X, Y, and Z axes,

$$\mathbf{x}(t) = \mathbf{Q}_{\rm X}(t)\mathbf{Q}_{\rm Y}(t)\mathbf{Q}_{\rm Z}(t)\mathbf{u}_{\rm VCG}(t), \tag{15}$$

where $\mathbf{u}_{\rm VCG}(t)$ is a 3×1 vector and the rotation matrices

$$\mathbf{Q}_{\rm X}(t) = \begin{bmatrix} 1 & 0 & 0 \\ 0 & \cos\varphi_{\rm X}(t) & \sin\varphi_{\rm X}(t) \\ 0 & -\sin\varphi_{\rm X}(t) & \cos\varphi_{\rm X}(t) \end{bmatrix}, \tag{16}$$

$$\mathbf{Q}_{\rm Y}(t) = \begin{bmatrix} \cos\varphi_{\rm Y}(t) & 0 & \sin\varphi_{\rm Y}(t) \\ 0 & 1 & 0 \\ -\sin\varphi_{\rm Y}(t) & 0 & \cos\varphi_{\rm Y}(t) \end{bmatrix}, \tag{17}$$

$$\mathbf{Q}_{\rm Z}(t) = \begin{bmatrix} \cos\varphi_{\rm Z}(t) & \sin\varphi_{Z}(t) & 0 \\ -\sin\varphi_{\rm Z}(t) & \cos\varphi_{\rm Z}(t) & 0 \\ 0 & 0 & 1 \end{bmatrix}, \tag{18}$$

are defined by the angular signals $\varphi_{\rm X}(t), \varphi_{\rm Y}(t)$, and $\varphi_{\rm Z}(t)$.

Introducing a template respiratory cycle $\psi(t)$, the angular variation is assumed to be proportional to the amount of air in the lungs, modeled as the product of two logistic functions accounting for inspiration and expiration [29], [30],

$$\psi(t; \delta_{\rm in}, \delta_{\rm ex}) = \frac{1}{1 + e^{-\gamma_{\rm in}(t-\delta_{\rm in})}} \frac{1}{1 + e^{\gamma_{\rm ex}(t-\delta_{\rm ex})}}, \tag{19}$$

where $\gamma_{\rm in}$ and $\gamma_{\rm ex}$ define the steepness of inspiration and expiration, respectively, and $\delta_{\rm in}$ and $\delta_{\rm ex}$ are positive-valued and uniformly distributed, defining the approximate duration of inspiration and expiration, respectively. The angular variation in each of the leads $o \in \{\rm X, Y, Z\}$ is modeled by

$$\varphi_o(t) = \xi_o \sum_{p=0}^{\infty} \alpha_{o,p} \psi\left(\frac{t - \sum_{q=0}^{p} T_{r,q}}{s_p}; \delta_{{\rm in},p}, \delta_{{\rm ex},p} \right), \tag{20}$$

where $\xi_o > 0$ is the maximum variation (expressed in degrees), $\alpha_{o,p}$ is a uniformly distributed amplitude, T_r is the duration of the template respiratory cycle, and $s_p = T_{r,p}/T_r$ is a scaling factor ensuring that the p:th cycle has the duration $T_{r,p}$.

B. Sinus Rhythm Influenced by Time-Varying Respiration

The HRV power spectrum is assumed to be composed of a Gaussian, related to baroreflex regulation ("LF component"), and another Gaussian, related to parasympathetic stimulation ("HF component") [23], see also [5]. For $\Omega \geq 0$, the time-varying power spectrum is defined by

$$S_{\rm RR}(t, \Omega) = \frac{P_{\rm LF}(t)}{\sqrt{2\pi\sigma_{\rm LF}^2}} e^{-\frac{(\Omega - 2\pi F_{\rm LF})^2}{2\sigma_{\rm LF}^2}} + \frac{P_{\rm HF}(t)}{\sqrt{2\pi\sigma_{\rm HF}^2}} e^{-\frac{(\Omega - 2\pi F_r(t))^2}{2\sigma_{\rm HF}^2}}, \tag{21}$$

and, due to symmetry, $S_{\rm RR}(t, \Omega) = S_{\rm RR}(t, -\Omega)$. The powers $P_{\rm LF}(t)$ and $P_{\rm HF}(t)$ and the center frequency of the HF component, set to the respiratory frequency $F_{\rm r}(t)$, are time-varying, whereas the widths $\sigma_{\rm LF}^2$ and $\sigma_{\rm HF}^2$ and the center frequency $F_{\rm LF}$ are time-invariant.

An RR interval signal $d_{\rm RR}(t)$, whose properties are described by (21), is generated by linear filtering of white noise $v_{\rm RR}(t)$ so that the LF component is the output of the time-invariant filter $h_{\rm LF}(t)$ and the HF component is the output of the time-varying filter $h_{\rm HF}(t; F_r(t))$,

$$d_{\rm RR}(t) = \left(\sqrt{P_{\rm LF}(t)} h_{\rm LF}(t) + \sqrt{P_{\rm HF}(t)} h_{\rm HF}(t; F_r(t)) \right) * v_{\rm RR}(t) + m_{\rm RR}(t). \tag{22}$$

The function $m_{\rm RR}(t)$ is the time-varying mean RR interval. Recalling that the power spectrum of filtered white noise, with variance $\sigma_{v,\rm RR}^2$ is given by $S_{\rm RR}(t, \Omega) = |H(t, \Omega)|^2 \sigma_{v,\rm RR}^2$, the frequency response $H(t, \Omega)$ is identified as the square root of a Gaussian in (21), which after use of the inverse Fourier transform results in the following two impulse responses:

$$h_{\rm LF}(t) = \sqrt[4]{\frac{32}{\pi^5}} \frac{\sqrt{\sigma_{\rm LF}}}{1 + 2\sigma_{\rm LF}^2 t^2} \cos(2\pi F_{\rm LF} t), \tag{23}$$

$$h_{\rm HF}(t; F_r(t)) = \sqrt[4]{\frac{32}{\pi^5}} \frac{\sqrt{\sigma_{\rm HF}}}{1 + 2\sigma_{\rm HF}^2 t^2} \cos(2\pi F_r(t) t). \tag{24}$$

The discrete-time implementation is accomplished by sampling each impulse response symmetrically around $t = 0$ until its envelope falls below 5% of its peak value; the same sampling rate as that of $d_{\rm RR}(t)$ and $F_r(t)$ is used. Since the filters $h_{\rm LF}(t)$ and $h_{\rm HF}(t; F_r(t))$ are noncausal, each filter needs to be shifted by half its length to become causal.

For a linearly increasing $F_r(t)$ and a linearly decreasing $m_{\rm RR}(t)$, the angular function $\varphi_{\rm X}(t)$ and the RR interval signal $d_{\rm RR}(t)$ are illustrated in Fig. 8(a) and (b), respectively. The resulting simulated ECG is illustrated in Fig. 8(c).

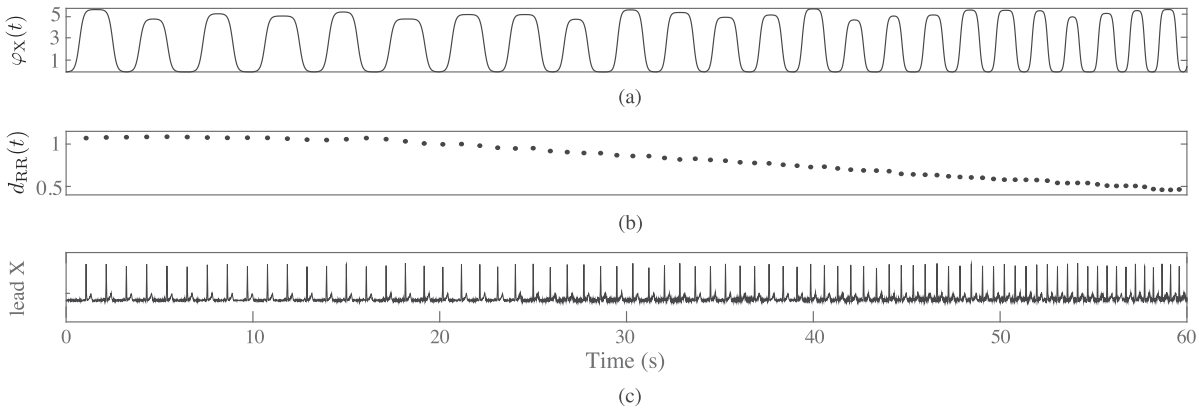

Fig. 8. Time-varying respiratory frequency, linearly increasing from 0.2 to 0.5 Hz in a 60-s interval, influencing (a) the angular function $\varphi_X(t)$ (radians), partially describing the variation in the electrical axis, (b) the variation in RR intervals, visible at the end of the RR interval signal $d_{RR}(t)$ (expressed in seconds), and (c) the simulated ECG in lead X. Noise level is gradually increasing to mimic an exercise stress test.

VIII. Modeling the Influence of Heart Rate on the PQ and QT Intervals

The proposed model accounts for the dependence of PQ and QT intervals on heart rate, both crucial to deal with when simulating ECGs in time-varying conditions.

A. PQ–RR Dependence

To account for the fact that the PQ interval depends on heart rate at higher heart rates, a simple nonlinear, memoryless model is introduced. The model builds on the physiological finding that the PR interval depends on heart rate at higher heart rates, while otherwise independent [31]. However, since the QR duration does not change significantly at higher heart rates [32], the dependence of the PQ interval $d_{PQ}(d_{RR}(k))$ on the preceding RR interval $d_{RR}(k)$ of the k:th beat can be modeled by the following expression:

$$d_{PQ}(d_{RR}(k)) = \begin{cases} d_{PQ_0} + \kappa_{PQ}(d_{RR}(k) - d_{RR,cp}), & d_{RR}(k) < d_{RR,cp}; \\ d_{PQ_0}, & d_{RR}(k) \geq d_{RR,cp}, \end{cases} \tag{25}$$

where d_{PQ_0} is the baseline PQ interval observed at lower heart rates, κ_{PQ} is the slope of the linear dependence, and $d_{RR,cp}$ is the change point for the dependence. Thus, assuming that P wave duration is independent of heart rate, P wave onset is positioned $d_{PQ}(d_{RR}(k))$ seconds before QRS onset.

The parameters d_{PQ_0}, κ_{PQ}, and $d_{RR,cp}$ can be estimated by analyzing the dependence between PQ and RR intervals in subjects performing exercise stress testing. Then, the range of RR intervals is divided into B_{RR} bins of equal width, and the median of the PQ intervals contained in each bin is computed, resulting in $d_{med}(b) \equiv d_{PQ}(d_{RR}(b)), b = 1, \ldots, B_{RR}$. The bin corresponding to the change point is estimated by minimizing the following LS error function with respect to b_0:

$$\varepsilon(b_0) = \sum_{b=1}^{b_0} w(b)(d_{med}(b) - d_{PQ_0} - \kappa_{PQ}(d_{RR}(b) - d_{RR,cp}))^2 + \sum_{b=b_0+1}^{B_{RR}} w(b)(d_{med}(b) - d_{PQ_0})^2, \tag{26}$$

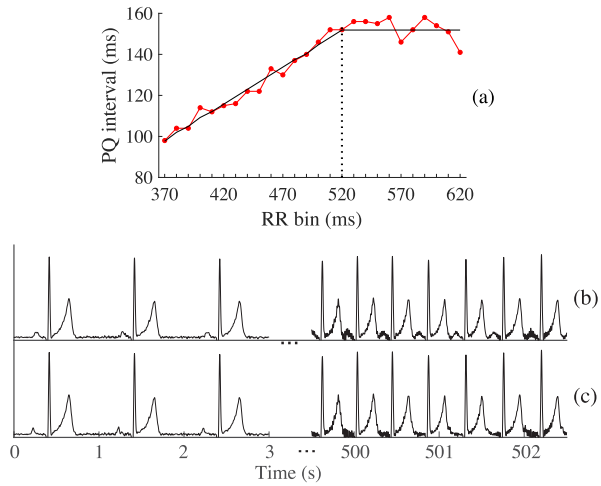

Fig. 9. (a) Median of the PQ intervals contained in each RR interval bin (red curve). Fitted function (black curve) is given by the estimates $\hat{d}_{PQ_0} = 152$ ms, $\hat{\kappa}_{PQ} = 0.358$, and $\hat{d}_{RR,cp} = 520$ ms; $\hat{d}_{RR,cp}$ is indicated by a vertical dotted line. (b) Simulated ECG with PQ–RR dependence modeled at low and high heart rates, and (c) simulated ECG without modeling of PQ–RR dependence, causing the P waves to be incorrectly hidden in the T-waves at a high heart rate.

thus yielding $\hat{d}_{RR,cp} = d_{RR}(\hat{b}_0)$. The weights $w(b)$ are taken as the number of subjects contributing to the b-th bin.

The estimation procedure is illustrated by analyzing ECGs recorded from healthy subjects performing exercise stress testing [33]. Following spatial periodic component analysis to improve the signal quality, the PQ interval was determined using wavelet-based delineation of P wave onset and QRS onset [34]. Fig. 9(a) shows the median of all PQ intervals in each of the RR interval bins to which the function in (25) is fitted. Fig. 9(b) and (c) show simulated ECGs with and without inclusion of PQ–RR dependence, respectively. Without PQ–RR dependence, P waves occur too far away from the QRS complex at high heart rates, thus not reflecting normal electrophysiological behavior.

B. QT–RR Adaptation

The lack of QT–RR adaptation was the main concern raised by the expert medical doctors when assessing the realism of simulated ECGs in [5]. This issue is addressed by introducing

an input–output model accounting for QT interval adaptation to RR interval changes [35]; the adaptation is composed of a fast, initial phase extending a few RR intervals and a slow phase lasting for several minutes [36].

Since the model operates on a sample-to-sample basis, the RR intervals $d_{\mathrm{RR}}(k)$ and the QT intervals $d_{\mathrm{QT}}(k)$ are both evenly resampled at a rate of 4 Hz, resulting in $x_{\mathrm{RR}}(n)$ and $x_{\mathrm{QT}}(n)$, respectively. The input–output relation between the preceding RR intervals and the QT interval is defined by a finite impulse response filter, whose output is denoted $x_{\overline{\mathrm{RR}}}(n)$, followed by a memoryless nonlinear function. The impulse response $h(n)$ is a truncated exponential,

$$h(n) = \frac{(1-\alpha_{\mathrm{QT}})}{(1-\alpha_{\mathrm{QT}}^{N})}\alpha_{\mathrm{QT}}^{n}, \quad n = 0, \ldots, N-1, \tag{27}$$

whose length N corresponds to 300 s based on physiological considerations. The exponential decay α_{QT} $(0 < \alpha_{\mathrm{QT}} < 1)$ is related to the time constant τ through $\alpha_{\mathrm{QT}} = e^{-\frac{1}{\tau}}$, where τ is set to 25 s [37]. Based on the results in [35], the model output $x_{\mathrm{QT}}(n)$ is taken to be inversely proportional to $x_{\overline{\mathrm{RR}}}(n)$,

$$x_{\mathrm{QT}}(n) = 0.49 - \frac{0.09}{x_{\overline{\mathrm{RR}}}(n)}. \tag{28}$$

The QT interval of the k:th beat is then modified by resampling the T wave while maintaining the QRS duration so that the QT interval becomes equal to that indicated by the model, where $d_{\mathrm{QT}}(k)$ is taken from the corresponding $x_{\mathrm{QT}}(n)$. The model for QT–RR adaptation has proven useful not only in SR [35] but also in AF [38].

IX. Validation of the Simulation Model

Unless specified in the following, the simulated ECGs are generated using the default parameter values listed in [16].

A. Signal Realism Assessed by Medical Doctors

The realism of the simulated ECGs was assessed using a dataset consisting of 100 15-s simulated, single-lead ECGs and another dataset consisting of 100 15-s real, single-lead ECGs recorded during either ambulatory monitoring, exercise stress testing and AF screening using a handheld device. Different lead positions were included. The datasets were approximately matched with regard to occurrence of arrhythmia and noise level. The datasets were presented blindly to three medical doctors with extensive experience in ECG interpretation, who were asked to identify the simulated ECGs.

B. Quality Control and Training Using Simulated ECGs

Simulator usefulness is illustrated by a signal quality control problem of identifying transient noise, abundant in AF screening, with the aim to reduce the number of falsely detected beats. The problem was addressed using a convolutional neural network (CNN) [39] to exclude false beat detections from the RR interval series before performing rhythm-based AF detection [40]. Training of the CNN was based on a subset of 30-s ECGs of the StrokeStop I screening database [41], where detected events outputted by a QRS detector was manually annotated as true or false. A disjoint subset of the StrokeStop I database was then used for testing, manually annotated by experts to confirm AF in the presence of noise, artifacts, and other non-AF arrhythmias.

TABLE I
Outcome of Realism Assessment Based on Real and Simulated ECGs

	Assessed as realistic
100 real ECGs	**84** (91/80/81)
100 simulated ECGs	**79** (90/63/84)

The boldface number is the average of the numbers within parenthesis produced by three medical doctors.

Exactly the same problem is addressed here, except that simulated ECGs are used instead for training. The training set consists of true and false beat detections, produced using (13) with two different settings of p_b and σ_z^2, defining the Bernoulli–Gaussian process, so that either low or high levels of motion artifacts result. The low level is given by uniform PDFs of p_b and σ_z^2 defined by the intervals $[0.001, 0.01]$ and $[0.01, 0.05]$, respectively, and the high level by uniform PDFs defined by $[0.1, 0.5]$ and $[0.05, 0.1]$, respectively. The overall muscle noise level m_{σ_w} is assigned a uniform PDF defined by $[10, 50]$ μV and $\sigma_v = 0$. While true beat detections are known from the simulation of the noise-free ECG, false detections are determined using a QRS detector: a detected event is deemed false whenever its occurrence time deviates more than 250 ms from that of a true beat detection. In total, 33,453 true detections and 10,498 false detections are obtained, i.e., about the same sizes as those used for training and validation in [39]. The simulated ECGs are composed of different combinations of SR, AT, AF, and bi- and trigeminy.

The CNN, trained on simulated ECGs, is tested on the above-mentioned, disjoint subset of the StrokeStop I database, using sensitivity (Se), false positive rate (FPR), and positive predictive value (PPV) to describe AF detection performance.

C. AF Detection and Training Using simulated/real ECGs

Another illustration of simulator usefulness is provided by addressing AF detection using a CNN either trained on simulated ECGs and tested on real ECGs, or vice versa. Thus, the approach taken here to AF detection differs from the one in Section IX-B which involves classical threshold testing. The data sets described in Section IX-A were employed for training and testing, though slightly modified to ensure that the same number of AF and non-AF records were included.

AF detection was based on a GoogleNet CNN fed with RGB scalograms, obtained by computing the continuous wavelet transform of the baseline-corrected and amplitude-normalized ECG. Since the training sets were small, they were augmented by randomly shifting each ECG 15 times in the range of 1 to 5 s. Moreover, the training sets were split by the ratio of 70:30, where 30% were used for validation.

Depending on the rhythm which dominated the 15-s record, each ECG was annotated as either AF or non-AF. Similar to Section IX-B, the detector output was compared to the annotations on a record basis.

X. Results

A. Signal Realism Assessed by Medical Doctors

The outcome of the assessment is presented in Table I. Ideally, from a simulation standpoint, the right column should be 100 to indicate that all ECGs, whether real or simulated, are assessed

TABLE II
QUALITY CONTROL AND RELATED AF DETECTION PERFORMANCE, EXPRESSED IN TERMS OF SENSITIVITY (SE), FALSE POSITIVE RATE (FPR), AND POSITIVE PREDICTIVE VALUE (PPV)

	Se (%)	FPR (%)	PPV (%)
CNN-based quality control trained on simulated ECGs	98.5	68.9	5.8
CNN-based quality control trained on real ECGs [40]	99.0	65.0	6.2
No quality control [40]	99.0	87.5	4.6

TABLE III
AF DETECTION PERFORMANCE IN TERMS OF SE, FPR, AND PPV

	Se (%)	FPR (%)	PPV (%)
CNN-based AF detection trained on simulated ECGs	62.0	20.0	75.6
CNN-based AF detection trained on real ECGs	62.7	16.3	80.0

as realistic. The results in Table I show that the simulated ECGs exhibit considerable realism since the average number assessed as realistic (79 out 100) is about the same as that of real ECGs (84 out of 100). The assessment of doctor #2 deviates from those of the other two doctors as more simulated ECGs are assessed as unrealistic.

B. Quality Control and Training Using Simulated ECGs

Table II presents AF detection performance when either real or simulated ECGs are used for training of the CNN for quality control. Using simulated ECGs, a slight decrease in the sensitivity results (0.5%), while FPR increases by 3.9%. Nonetheless, compared to the performance obtained without quality control, the improvement is still substantial.

C. AF Detection and Training Using simulated/real ECGs

Table III shows that the CNN-based AF detector performs equally when simulated and real ECGs are used for training, although real ECGs yield a modest increase in FPR and PPV; the resulting performance is further discussed below.

XI. DISCUSSION

Simulation models have gone through a renaissance in recent years thanks to the introduction of generative adversarial network (GAN) models in machine learning. Such models can generate ECGs indistinguishable from real ones—an achievement which has proven useful for improving classification and denoising performance [42], [43]. When the aim is to understand how algorithmic performance is influenced by various factors such as the influence of f-waves on ECG-derived respiration [44] or the influence of different lead transformations on the delineation of the QT interval in the presence of AF [38], the proposed simulator offers intuitive control of such factors through mathematical modeling, while no such control is offered by current GAN models.

An important incentive for pursuing the present study is the simulation of ECGs exhibiting a higher degree of complexity/variability than those of the simulator in [5]. This is achieved by modeling arrhythmias other than SR and AF and by introducing time-varying signal and noise characteristics. In doing so, the simulated ECGs are expected to have a broad applicability in the realm of ECG analysis, especially when robust detection and estimation methods are to be designed. While the higher degree of detail advances the realism of simulated ECGs mimicking those observed during AF screening and monitoring, the achieved degree is likely insufficient to simulate ECGs observed during drug evaluation, calling for modeling of additional physiological factors.

The proposed modeling framework, building on a discrete-time Markov chain, is easily expanded to include other arrhythmias than those considered. The Markov chain is defined so that any arrhythmia must be followed by SR, representing a means to hold down the number of transition probabilities to be set. This particular definition facilitates the modeling of RR intervals inside an AT episode as they can be related to RR intervals in SR. Even if this definition influences to some extent the realism of the simulated ECGs, the evaluation of algorithmic performance is likely not much influenced by the transitions to SR, nor should be classifier training. However, if SR-transitioning is unacceptable, transition probabilities from one arrhythmia to another can be introduced. The Markov chain model is well-suited to handle switching between different rhythms with fixed burdens, whereas switching in the presence of gradually changing burdens calls for a more advanced Markov model with time-varying transition probabilities [45].

Noise represents an essential component of any ECG simulator. Noise recordings may be obtained from real ECGs that result from placing electrodes on the limbs in positions where only noise is visible; the most well-known collection of such noise recordings is the NSTDB. Another approach is to subtract the cardiac activity from real ECGs using an average [26] or median [46] beat, possibly in combination with a technique to reduce the influence of QRS-related residuals [26]. Ideally, these two approaches produce realistic noise, however, the electrodes may not necessarily be placed at positions where the cardiac activity is absent (in fact, residual activity can be observed in some of the motion artifact recordings of the NSTDB), nor does the average/median beat offer sufficient cancellation of the cardiac activity when, e.g., ectopic beats occur or the influence of respiration is large [10]. Another disadvantage is the half-hour duration of the noise recordings, with implications on simulation uniqueness. On the other hand, the proposed statistical noise model can generate recordings of any length and offers control of time-varying noise characteristics such as the power spectrum of muscle noise and the shape/intensity of motion artifacts.

Of the three main types of noise, i.e., baseline wander, muscle noise, and motion artifacts, the first-mentioned is the least critical to model and therefore not considered in the present study. Filtered-noise models of baseline wander range from linear, time-invariant, lowpass filtering [47] to time-varying AR modeling [1], [2]; in both these cases, the input noise to the linear system is white and Gaussian

The starting point of ECG simulation in [5] was the leads X, Y, and Z to which noise was added, then transformed by the Dower matrix to obtain the 12-lead ECG. Using the two-lead NSTDB, lead Z was derived from leads X and Y by means of

a memoryless, nonlinear transformation. When evaluating performance, e.g., that of multi-lead principal component analysis for f wave extraction [10], the results may be misleading due to the artificially introduced interlead correlation. Using instead the proposed noise model, not only is spatially uncorrelated noise easily generated, but so can partially correlated noise, e.g., motion artifacts occurring at the same time in different leads but with shapes that differ between leads thanks to the stochastic impulse response in (11); use of the latter case requires a minor modification of the noise model.

Several simulator parameters have been assigned default values derived from the thoroughly annotated MITADB, which, despite its limited size, is commonly used for research in ECG analysis. As a result, the simulator attempts to capture the physiological variability of MITADB. In addition, the simulator features models developed using other databases as well as established medical knowledge.

The question 'Does the simulation model generate realistic ECGs?' is not easily answered due to the difficulty to define a ground truth to which the simulated ECGs can be assessed. One answer is to let experienced medical doctors assess the realism of simulated ECGs. While the significance of such an assessment should not be exaggerated, it nonetheless provides an indication of whether essential features are captured by the simulated ECGs. Indeed, Table I shows that the doctors had difficulties to distinguish simulated from real ECGs as the number of simulated ECGs assessed as realistic does not differ that much from the number of real ECGs assessed as realistic. The main reason simulated ECGs are assessed as unrealistic is due to that certain VPBs had too long coupling intervals and too low QRS amplitudes—issues which are easily addressed using other model parameter values, possibly in combination with non-uniform PDFs of the β_{VPB}-parameters. The number of simulated ECGs assessed as unrealistic due to noise and artifacts was about the same as the corresponding one of real ECGs, and, therefore, it may be concluded that the noise models are realistic.

Table II demonstrates the potential of using simulated ECGs to train a CNN so that false detections can be excluded before AF detection takes place: the performance is essentially the same irrespective of whether real or simulated ECGs are used for training. The slight difference may be attributed to the noise/artifact models and a too limited variability in beat morphology. Indeed, screening for AF is a scenario where sparse, imbalanced data is typically encountered, exemplified by a study where 278 out of 80,149 ECGs were interpreted as AF [41]. To address this dramatic imbalance when training a CNN, the AF data set can be augmented with simulated ECGs with similar characteristics with respect to, e.g., AF burden, APB and VPB occurrence, and noise.

The poor AF detection performance presented in Table III is largely explained by the facts that training and testing is performed on different data sets, small data sets contain varying leads, and considerable signal complexity due to the presence of various non-AF arrhythmias. However, these results should be viewed in light of the survey recently presented in [9] which shows that a large number of studies reporting near-perfect AF detection performance make use of the same database for training and testing and include the same patient in both the training and the test sets. Concerning simulator usefulness, the results in Table III which show that training using real ECGs does not offer much better performance than does training using simulated ECGs suggest that the simulated ECGs are realistic.

XII. Conclusion

The proposed ECG simulator advances the modeling of arrhythmias and noise/artifacts by introducing time-varying signal characteristics with the aim to increase signal complexity. The three-part validation suggests that the simulated ECGs are realistic and therefore of use for the evaluation of algorithmic performance in various applications. Such applications include data augmentation of incomplete databases and benchmarking of algorithms, e.g., for arrhythmia detection, noise detection, ECG-derived respiration, and QT–RR adaptation.

Appendix A
Transition Probabilities of the Markov Chain Model

The transition probabilities of the Markov chain model in Section II can alternatively be defined in terms of rhythm burden and mean episode duration, applying to each of the arrhythmias in the set $G = \{\text{AT}, \text{AF}, \text{BT}, \text{VPB}\}$. The rhythm burden B_g is defined as the ratio of the expected arrhythmia duration T_g and the total duration T of the simulated ECG,

$$B_g = \frac{T_g}{T}, \quad g \in G. \tag{29}$$

The mean episode duration e_g, expressed in number of beats, is determined from the PMFs $p_g(l)$, except for a VPB which is a single-beat arrhythmia and therefore $e_{\text{VPB}} = 1$. Moreover, the average RR interval $\bar{d}_{\text{RR},g}$, expressed in seconds, is needed which, depending on arrhythmia, is determined by the models in Section VII-B and [5], except for the average RR interval $\bar{d}_{\text{RR,VPB},g}$ of a VPB occurring in $g \in \{\text{SR}, \text{AT}, \text{AF}\}$ which is determined by the RR interval preceding the VPB.

Although SR is not an arrhythmia, its presence is, in the name of conformity, also associated with a "burden", given by

$$B_{\text{SR}} = \frac{n_{\text{SR}}\, e_{\text{SR}}\, \bar{d}_{\text{RR,SR}}}{T}, \tag{30}$$

where n_{SR} is the number of SR episodes and e_{SR} is the mean of the exponentially distributed SR episode duration (expressed in beats). By definition, the rhythm burdens sum to one,

$$B_{\text{SR}} + B_{\text{AT}} + B_{\text{AF}} + B_{\text{BT}} + B_{\text{VPB}} = 1. \tag{31}$$

The BT burden, unlinked to a VPB state, is given by

$$B_{\text{BT}} = \frac{n_{\text{SR}}\, p_{\text{SR}\to\text{BT}}\, e_{\text{BT}}\, \bar{d}_{\text{RR,BT}}}{T}, \tag{32}$$

where $p_{\text{SR}\to\text{BT}}$ is the transition probability between SR and BT. Similar to (30), the AT and AF burdens are given by

$$B_{\text{AT}} = \frac{n_{\text{AT}}\, e_{\text{AT}}\, \bar{d}_{\text{RR,AT}}}{T}, \tag{33}$$

$$B_{\text{AF}} = \frac{n_{\text{AF}}\, e_{\text{AF}}\, \bar{d}_{\text{RR,AF}}}{T}, \tag{34}$$

where n_{AT} and n_{AF} are the number of AT and AF episodes, respectively. The burden of the VPB states is split between the SR, AT, and AF states, proportionally to B_{SR}, B_{AT} and B_{AF}:

$$B_{\text{VPB}} = B_{\text{VPB,SR}} + B_{\text{VPB,AT}} + B_{\text{VPB,AF}}, \tag{35}$$

$$B_{\text{VPB,g}} = \frac{n_g\, p_{g\to\text{VPB}}\, \bar{d}_{\text{RR,VPB},g}}{T}, \quad g \in \{\text{SR}, \text{AT}, \text{AF}\}, \tag{36}$$

where $\bar{d}_{\mathrm{RR,VPB,g}}$ depends on $\beta_{\mathrm{VPB,p}}$ and $\beta_{\mathrm{VPB,f}}$ introduced in Section IV-A. Before the transition probabilities can be determined, n_{SR}, n_{AT}, n_{AF}, and d_{SR} need to be determined, whereas T, e_g, and $\bar{d}_{\mathrm{RR},g}$ for $g \in \{\mathrm{SR}, \mathrm{AT}, \mathrm{AF}\}$ are assumed to be known. The probabilities $p_{\mathrm{BT}\to\mathrm{SR}}$, $p_{\mathrm{VPB}\to\mathrm{SR}}$, $p_{\mathrm{VPB}\to\mathrm{AT}}$, and $p_{\mathrm{VPB}\to\mathrm{AF}}$ are always set to 1.

The number of AT and AF episodes can be related to the other variables by realizing that the number of transitions to either the AT states or the AF states is the sum of the transitions from the SR state and the respective VPB states:

$$n_{\mathrm{AT}} = n_{\mathrm{SR}}\, p_{\mathrm{SR}\to\mathrm{AT}} + n_{\mathrm{AT}}\, p_{\mathrm{AT}\to\mathrm{VPB}}, \tag{37}$$

$$n_{\mathrm{AF}} = n_{\mathrm{SR}}\, p_{\mathrm{SR}\to\mathrm{AF}} + n_{\mathrm{AF}}\, p_{\mathrm{AF}\to\mathrm{VPB}}. \tag{38}$$

The number of SR episodes is determined by the insight that the transition probabilities from SR to any of the arrhythmias in G must sum to one,

$$p_{\mathrm{SR}\to\mathrm{VPB}} + p_{\mathrm{SR}\to\mathrm{AT}} + p_{\mathrm{SR}\to\mathrm{AF}} + p_{\mathrm{SR}\to\mathrm{BT}} = 1. \tag{39}$$

Using the above equations, n_{SR} is found to be

$$\begin{aligned} n_{\mathrm{SR}} = {} & \frac{B_{\mathrm{AT}}\bar{d}_{\mathrm{RR,VPB,AT}}T - B_{\mathrm{VPB,AT}}e_{\mathrm{AT}}\bar{d}_{\mathrm{RR,AT}}T}{\bar{d}_{\mathrm{RR,VPB,AT}}e_{\mathrm{AT}}\bar{d}_{\mathrm{RR,AT}}} + \frac{B_{\mathrm{BT}}T}{e_{\mathrm{BT}}\bar{d}_{\mathrm{RR,BT}}} \\ & + \frac{B_{\mathrm{AF}}\bar{d}_{\mathrm{RR,VPB,AF}}T - B_{\mathrm{VPB,AF}}e_{\mathrm{AF}}\bar{d}_{\mathrm{RR,AF}}T}{\bar{d}_{\mathrm{RR,VPB,AF}}e_{\mathrm{AF}}\bar{d}_{\mathrm{RR,AF}}} \\ & + \frac{B_{\mathrm{VPB,SR}}T}{\bar{d}_{\mathrm{RR,VPB,SR}}\bar{d}_{\mathrm{RR,SR}}}. \end{aligned} \tag{40}$$

Due to the minus sign in the numerator of the first and third addends, $B_{\mathrm{VPB,AT}}$ and $B_{\mathrm{VPB,AF}}$ need to be constrained by a threshold that depends on B_{AT} and B_{AF}, respectively, to avoid a negative n_{SR}. The mean SR episode duration is given by

$$e_{\mathrm{SR}} = \max\left(\frac{TB_{\mathrm{SR}}}{n_{\mathrm{SR}}\bar{d}_{\mathrm{RR,SR}}}, 1\right). \tag{41}$$

The desired transition probabilities are determined from (32), (33), (34), (36), (37), and (38) together with that both $p_{\mathrm{AT}\to\mathrm{SR}} + p_{\mathrm{AT}\to\mathrm{VPB}}$ and $p_{\mathrm{AF}\to\mathrm{SR}} + p_{\mathrm{AF}\to\mathrm{VPB}}$ are equal to 1.

Appendix B
Fitting Hermite functions

Estimation of the Hermite function parameters τ and σ is easily accomplished by the grid search minimization proposed below. By including the logistic function in the model, a five-dimensional minimization problem arises which here is solved by an iterative, LS-based, two-step estimation procedure where estimation of the Hermite parameters is followed by estimation of the logistic parameters c_s, τ_s, and σ_s, then repeated until a stopping criterion is met. Although the procedure is suboptimal, it has been found to converge to parameter estimates which provide an excellent fit.

0. The isolectric segment of each beat is set to zero by subtracting the amplitude just before Q wave onset. The procedure is initiated by $\hat{c}_{s,0} = 0$ and $i = 1$.
1. Let $y_i(t)$ be the "jump-corrected" observed signal $x(t)$,

$$y_i(t) = x(t) - s(t; \hat{c}_{s,i-1}, \hat{\tau}_{s,i-1}, \hat{\sigma}_{s,i-1}). \tag{42}$$

Then, τ and σ are estimated using the LS criterion

$$[\hat{\tau}_i, \hat{\sigma}_i] = \arg\min_{\tau,\sigma} \left| y_i(t) - \sum_{j=0}^{J-1} c_{j,i}(\tau,\sigma)\varphi_j\left(t-\tau,\sigma\right) \right|^2, \tag{43}$$

where the amplitudes $c_{j,i}(\tau,\sigma)$ are easily determined thanks to orthonormality,

$$c_{j,i}\left(\tau,\sigma\right) = \int_{-\infty}^{+\infty} y_i(t)\varphi_j(t-\tau,\sigma)dt. \tag{44}$$

2. The parameters defining the logistic function are estimated by minimizing the LS criterion

$$[\hat{c}_{s,i}, \hat{\tau}_{s,i}, \hat{\sigma}_{s,i}] = \arg\min_{c_s,\tau_s,\sigma_s} \left| e_i(t) - s(t; c_s, \tau_s, \sigma_s,) \right|^2, \tag{45}$$

where $e_i(t) = x(t) - \sum_j c_{j,i}(\hat{\tau},\hat{\sigma})\varphi_j(t-\hat{\tau},\hat{\sigma})$. To ensure that the QRS-to-T transition at time t_p is smooth, $\hat{c}_{s,i}^{(\mathrm{QRS})}$ and $\hat{c}_{s,i}^{(\mathrm{T})}$ must have the same value, accomplished by the following modification:

$$\hat{c}_{s,i}^{(\mathrm{w})} = \frac{s\left(t_p; \hat{c}_{s,i}^{(\mathrm{QRS})}, \hat{\tau}_{s,i}^{(\mathrm{QRS})}, \hat{\sigma}_{s,i}^{(\mathrm{QRS})}\right) + s\left(t_p; \hat{c}_{s,i}^{(\mathrm{T})}, \hat{\tau}_{s,i}^{(\mathrm{T})}, \hat{\sigma}_{s,i}^{(\mathrm{T})}\right)}{2s(t_p; 1, \hat{\tau}_{s,i}^{(\mathrm{w})}, \hat{\sigma}_{s,i}^{(\mathrm{w})})}, \tag{46}$$

where $\mathrm{w} \in \{\mathrm{QRS,T}\}$. Using the resulting estimates, the fitted function is given by

$$\hat{x}(t) = \sum_{j=0}^{J-1} c_{j,i}(\hat{\tau}_i, \hat{\sigma}_i)\varphi_j\left(t-\hat{\tau}_i, \hat{\sigma}_i\right) - \hat{c}_{s,i}s(\hat{\sigma}_{s,i}(t-\hat{\tau}_{s,i})). \tag{47}$$

yielding the LS error $\varepsilon_i = |x(t) - \hat{x}(t)|^2$.
3. The iterations are stopped when ε_i drops below a certain threshold (typically already after one or two iterations), no longer improves after a certain number of iterations, or when $\hat{c}_{s,i}^{(\mathrm{QRS})}$ and $\hat{c}_{s,i}^{(\mathrm{T})}$ have opposite signs. If none of these criteria is fulfilled, $i = i + 1$, step 1 is repeated.

The estimates $\hat{c}_0 = c_0(\hat{\sigma},\hat{\tau}), \ldots, \hat{c}_{J-1} = c_{J-1}(\hat{\sigma},\hat{\tau})$, $\hat{\sigma}$, $\hat{\tau}$, $\hat{c}_s$, $\hat{\sigma}_s$, and $\hat{\tau}_s$ are saved in a library of synthesized VPBs.

For the 987 low-noise 12-lead VPBs extracted from the INCART database [17] and saved in the library, $J = 6$ functions were fitted to the QRS and $J = 4$ functions to the T wave of each lead, resulting in an average fitting error of 5.4% irrespective of whether the logistic function was used or not. Thus, VPBs can be modeled by Hermite functions alone.

Acknowledgment

The authors would like to thank Dr. Maurizio Varanini and Dr. Lucia Billeci, Institute of Clinical Physiology, National Council of Research of Italy, for their support of the project.

References

[1] R. Sameni et al., "Multichannel ECG and noise modeling: Application to maternal and fetal ECG signals," *J. Adv. Signal Process.*, vol. 2007, pp. 1–14, 2007.

[2] J. Behar et al., "An ECG simulator for generating maternal-foetal activity mixtures on abdominal ECG recordings," *Physiol. Meas.*, vol. 35, pp. 1537–1550, 2014.

[3] E. Keenan, C. K. Karmakar, and M. Palaniswami, "The effects of asymmetric volume conductor modeling on non-invasive fetal ECG extraction," *Physiol. Meas.*, vol. 39, 2018, Art. no. 105013.

[4] G. D. Clifford, S. Nemati, and R. Sameni, "An artificial vector model for generating abnormal electrocardiographic rhythms," *Physiol. Meas.*, vol. 31, pp. 595–609, 2010.

[5] A. Petrėnas et al., "Electrocardiogram modeling during paroxysmal atrial fibrillation: Application to the detection of brief episodes," *Physiol. Meas.*, vol. 38, pp. 2058–2080, 2017.

[6] G. Luongo et al., "Hybrid machine learning to localize atrial flutter substrates using the surface 12-lead electrocardiogram," *Europace*, vol. 24, pp. 1186–1194, 2022.

[7] A. Sološenko et al., "Training neural networks on simulated data: Application to bradycardia and tachycardia detection," *Front. Physiol.*, vol. 13, 2022, Art. no. 928098.

[8] A. Petrėnas et al., "Detection of occult paroxysmal atrial fibrillation," *Med. Biol. Eng. Comput.*, vol. 53, pp. 287–297, 2015.

[9] M. Butkuvienė et al., "Considerations on performance evaluation of atrial fibrillation detectors," *IEEE Trans. Biomed. Eng.*, vol. 68, no. 11, pp. 3250–3260, Nov. 2021.

[10] L. Sörnmo, Ed., *Atrial Fibrillation From an Engineering Perspective*. Berlin, Germany: Springer, 2018.

[11] R. Alcaraz, L. Sörnmo, and J. J. Rieta, "Reference database and performance evaluation of methods for extraction of atrial fibrillatory waves in the ECG," *Physiol. Meas.*, vol. 40, 2019, Art. no. 75011.

[12] S. Mihandoust et al., "A comparative study of the performance of methods for F-wave extraction," *Physiol. Meas.*, vol. 43, 2022, Art. no. 105006.

[13] S. Kochhäuser et al., "Supraventricular premature beats and short atrial runs predict atrial fibrillation in continuously monitored patients with cryptogenic stroke," *Stroke*, vol. 45, pp. 884–886, 2014.

[14] B. Strøier Larsen et al., "Excessive atrial ectopy and short atrial runs increase the risk of stroke beyond incident atrial fibrillation," *J. Amer. College Cardiol.*, vol. 66, pp. 232–241, 2015.

[15] Y. Tian et al., "Modeling and reproducing textile sensor noise: Implications for textile-compatible signal processing algorithms," *IEEE J. Biomed. Health Inform.*, vol. 26, no. 1, pp. 243–253, Jan. 2022.

[16] L. Bachi et al., "ECG modeling for simulation of arrhythmias in time-varying conditions," Jun. 18, 2023. [Online]. Available: https://github.com/LorenzoBachi/simECG_2022

[17] A. L. Goldberger et al., "PhysioBank, PhysioToolkit, and PhysioNet: Components of a new research resource for complex physiologic signals," *Circulation*, vol. 101, pp. e215–e220, 2000.

[18] T. B. Garcia and D. J. Garcia, *Arrhythmia Recognition: The Art of Interpretation*, 2nd ed. Burlington, MA, USA: Jones & Bartlett Learn., 2019.

[19] L. Sörnmo et al., "A method for evaluation of QRS shape features using a mathematical model for the ECG," *IEEE Trans. Biomed. Eng.*, vol. 28, no. 10, pp. 713–717, Oct. 1981.

[20] P. Laguna et al., "Adaptive estimation of QRS complex by the Hermite model for classification and ectopic beat detection," *Med. Biol. Eng. Comput.*, vol. 34, pp. 58–68, 1996.

[21] M. Lagerholm et al., "Clustering ECG complexes using Hermite functions and self-organizing maps," *IEEE Trans. Biomed. Eng.*, vol. 47, no. 7, pp. 838–848, Jul. 2000.

[22] S. Suppappola, Y. Sun, and S. Chiaramida, "Gaussian pulse decomposition: An intuitive model of electrocardiogram waveforms," *Ann. Biomed. Eng.*, vol. 25, no. 2, pp. 252–260, 1997.

[23] P. E. McSharry et al., "A dynamical model for generating synthetic electrocardiogram signals," *IEEE Trans. Biomed. Eng.*, vol. 50, no. 3, pp. 289–294, Mar. 2003.

[24] C. Böck et al., "ECG beat representation and delineation by means of variable projection," *IEEE Trans. Biomed. Eng.*, vol. 68, no. 10, pp. 2997–3008, Oct. 2021.

[25] J. A. Kors et al., "Reconstruction of the Frank vectorcardiogram from standard electrocardiographic leads: Diagnostic comparison of different methods," *Eur. Heart J.*, vol. 11, pp. 1083–1092, 1990.

[26] R. Bailón et al., "Coronary artery disease diagnosis based on exercise ECG indexes from repolarization, depolarization and heart rate variability," *Med. Biol. Eng. Comput.*, vol. 41, pp. 561–571, 2003.

[27] J. M. Mendel, *Optimal Seismic Deconvolution. An Estimation-Based Approach*. New York, NY, USA: Academic, 1983.

[28] L. Sörnmo and P. Laguna, *Bioelectrical Signal Processing in Cardiac and Neurological Applications*. Amsterdam, The Netherlands: Elsevier, 2005.

[29] M. Åström et al., "Vectorcardiographic loop alignment and the measurement of morphologic beat-to-beat variability in noisy signals," *IEEE Trans. Biomed. Eng.*, vol. 47, no. 4, pp. 497–506, Apr. 2000.

[30] R. Bailón, L. Sörnmo, and P. Laguna, "A robust method for ECG-based estimation of the respiratory frequency during stress testing," *IEEE Trans. Biomed. Eng.*, vol. 53, no. 7, pp. 1273–1285, Jul. 2006.

[31] J.-H. Atterhög and E. Loogna, "PR interval in relation to heart rate during exercise and the influence of posture and autonomic tone," *J. Electrocardiol.*, vol. 10, no. 4, pp. 331–336, 1977.

[32] M. Pilhall, M. Riha, and S. Jern, "Changes in the QRS segment during exercise: Effects of acute β-blockade with propranolol," *Clin. Physiol.*, vol. 13, pp. 113–131, 1993.

[33] M. Virtanen et al., "Heart rate variability derived from exercise ECG in the detection of coronary artery disease," *Physiol. Meas.*, vol. 28, pp. 1189–1200, 2007.

[34] C. Pérez et al., "Eigenvector-based spatial ECG filtering improves QT delineation in stress test recordings," in *Proc. Asilomar Conf. Signals, Syst., Comput.*, vol. 55, 2021, pp. 261–264.

[35] E. Pueyo et al., "Characterization of QT interval adaptation to RR interval changes and its use as a risk-stratifier of arrhythmic mortality in amiodarone-treated survivors of acute myocardial infarction," *IEEE Trans. Biomed. Eng.*, vol. 51, no. 9, pp. 1511–1520, Sep. 2004.

[36] C. P. Lau et al., "Hysteresis of the ventricular paced QT interval in response to abrupt changes in pacing rate," *Cardiovasc. Res.*, vol. 22, pp. 67–72, 1988.

[37] C. Pérez et al., "Characterization of impaired ventricular repolarization by quantification of QT delayed response to heart rate changes in stress test," in *Proc. Comput. Cardiol.*, 2020, pp. 1–4.

[38] A. Martín-Yebra, L. Sörnmo, and P. Laguna, "QT interval adaptation to heart rate changes in atrial fibrillation as a predictor of sudden cardiac death," *IEEE Trans. Biomed. Eng.*, vol. 69, no. 10, pp. 3109–3118, Oct. 2022.

[39] H. Halvaei et al., "Identification of transient noise to reduce false detections in screening for atrial fibrillation," *Front. Physiol.*, vol. 12, 2021, Art. no. 672875.

[40] A. Petrėnas, V. Marozas, and L. Sörnmo, "Low-complexity detection of atrial fibrillation in continuous long-term monitoring," *Comput. Biol. Med.*, vol. 65, pp. 184–191, 2015.

[41] E. Svennberg et al., "Mass screening for untreated atrial fibrillation: The STROKESTOP study," *Circulation*, vol. 131, pp. 2176–2184, 2015.

[42] T. Golany, D. Freedman, and K. Radinsky, "SimGANs: Simulator-based generative adversarial networks for ECG synthesis to improve deep ECG classification," in *Proc. 37th Int. Conf. Mach. Learn.*, 2020, pp. 3597–3606.

[43] P. Singh and G. Pradhan, "A new ECG denoising framework using generative adversarial network," *IEEE/ACM Trans. Comput. Biol. Bioinform.*, vol. 18, no. 2, pp. 759–764, Mar./Apr. 2021.

[44] S. Kontaxis et al., "ECG-derived respiratory rate in atrial fibrillation," *IEEE Trans. Biomed. Eng.*, vol. 67, no. 3, pp. 905–914, Mar. 2020.

[45] M. Bazzi et al., "Time-varying transition probabilities for Markov regime switching models," *J. Time Ser. Anal.*, vol. 38, pp. 458–478, 2017.

[46] L. Galeotti and C. G. Scully, "A method to extract realistic artifacts from electrocardiogram recordings for robust algorithm testing," *J. Electrocardiol.*, vol. 51, pp. S56–S60, 2018.

[47] L. Sörnmo, "Time-variable digital filtering of ECG baseline wander," *Med. Biol. Eng. Comput*, vol. 31, pp. 503–508, 1993.